PNAS RESEARCH ARTICLE | BIOPHYSICS AND COMPUTATIONAL BIOLOGY

Structural insights into the activation of autoinhibited human lipid flippase ATP8B1 upon substrate binding

Meng-Ting Cheng[a,b,c,1], Yu Chen[a,b,c,1], Zhi-Peng Chen[a,b,c], Xin Liu[d], Zhiyong Zhang[d,e], Yuxing Chen[a,b,c,2], Wen-Tao Hou (侯文韬)[a,b,c,2], and Cong-Zhao Zhou[a,b,2]

Edited by John Rubinstein, Hospital for Sick Children, Toronto, Canada; received October 11, 2021; accepted February 24, 2022 by Editorial Board Member Yifan Cheng

The human P4 ATPase ATP8B1 in complex with the auxiliary noncatalytic protein CDC50A or CDC50B mediates the transport of cell-membrane lipids from the outer to the inner membrane leaflet, which is crucial to maintain the asymmetry of membrane lipids. Its dysfunction usually leads to an imbalance of bile-acid circulation and eventually causes intrahepatic cholestasis diseases. Here, we found that both ATP8B1–CDC50A and ATP8B1–CDC50B possess a higher ATPase activity in the presence of the most favored substrate phosphatidylserine (PS), and, moreover, that the PS-stimulated activity could be augmented upon the addition of bile acids. The 3.4-Å cryo-electron microscopy structures of ATP8B1–CDC50A and ATP8B1–CDC50B enabled us to capture a phosphorylated and autoinhibited state, with the N- and C-terminal tails separately inserted into the cytoplasmic interdomain clefts of ATP8B1. The PS-bound ATP8B1–CDC50A structure at 4.0-Å resolution indicated that the autoinhibited state could be released upon PS binding. Structural analysis combined with mutagenesis revealed the residues that determine the substrate specificity and a unique positively charged loop in the phosphorylated domain of ATP8B1 for the recruitment of bile acids. Together, we supplemented the Post–Albers transport cycle of P4 ATPases with an extra autoinhibited state of ATP8B1, which could be activated upon substrate binding. These findings not only provide structural insights into the ATP8B1-mediated restoration of human membrane lipid asymmetry during bile-acid circulation, but also advance our understanding of the molecular mechanism of P4 ATPases.

ATP8B1 | P4 ATPase | phospholipid flippase | bile acid | cryo-EM structure

Significance

ATP8B1 is a P4 ATPase that maintains membrane asymmetry by transporting phospholipids across the cell membrane. Disturbance of lipid asymmetry will lead to the imbalance of the cell membrane and eventually, cell death. Thus, defects in ATP8B1 are usually associated with severe human diseases, such as intrahepatic cholestasis. The present structures of ATP8B1 complexed with its auxiliary noncatalytic partners CDC50A and CDC50B reveal an autoinhibited state of ATP8B1 that could be released upon substrate binding. Moreover, release of this autoinhibition could be facilitated by the bile acids, which are key factors that alter the membrane asymmetry of hepatocytes. This enabled us to figure out a feedback loop of bile acids and lipids across the cell membrane.

The eukaryotic cell membrane consists of a variety of lipids, which are asymmetrically distributed across the lipid bilayer (1). Phosphatidylcholine (PC), sphingomyelin (SM), and glycolipids are enriched at the outer leaflet of the plasma membrane, whereas phosphatidylserine (PS), phosphatidylethanolamine (PE), and phosphatidylinositol (PI) are mainly restricted to the inner leaflet. The asymmetric distribution of lipids is essential to maintain cellular functions, including cell and organelle shape determination and dynamics, vesicle budding and trafficking, membrane stability and impermeability, cell signaling, apoptosis, and homeostasis of bile and cholesterol (2, 3). The disturbance of lipid asymmetry will lead to the imbalance of cell membrane and eventually cell death. For instance, loss of PS asymmetry is an early indicator of cell apoptosis, as well as a signal to initiate blood clotting (4). To maintain membrane asymmetry, eukaryotic cells express a series of cooperatively functioning lipid transporters, such as scramblases, floppases, and flippases. Scramblases, which are energy-independent, drive bidirectional lipid scrambling in response to intracellular concentrations of Ca^{2+} (5); whereas floppases, which are usually ATP-binding cassette (ABC) transporters, mediate the unidirectional translocation of lipids from the inner to the outer leaflet of the membrane bilayer (6). In contrast, flippases are usually P-type Type IV ATPase (P4 ATPase for short) in eukaryotic cells, which transport phospholipids from the outer leaflet to the inner leaflet (3).

The widespread P-type ATPases, which are featured with a phosphorylated intermediate during the transport cycle (P stands for phosphorylation), catalyze the transport of ions, phospholipids, polyamines, or transmembrane (TM) helices by utilizing the energy of ATP hydrolysis (7–10). The human genome encodes a total of 14 P4 ATPase members, which are further grouped into P4A and P4B clades (11). For proper localization and integral function, members of a P4A clade should form a complex with an auxiliary noncatalytic protein of the CDC50 family (12). To date, three CDC50 paralogs (CDC50A, CDC50B, and CDC50C) have been identified in mammals (13). As reported, most human P4A ATPases could bind to only CDC50A (12, 14), whereas

Author contributions: M.-T.C. designed research; M.-T.C., Yu Chen, Z.-P.C., X.L., and Z.Z. performed research; M.-T.C., Yu Chen, and W.-T.H. analyzed data; and M.-T.C., Yuxing Chen, W.-T.H., and C.-Z.Z. wrote the paper.

The authors declare no competing interest.

This article is a PNAS Direct Submission. J.R. is a guest editor invited by the Editorial Board.

[1]M.-T.C. and Yu Chen contributed equally to this work.

[2]To whom correspondence may be addressed. Email:cyxing@ustc.edu.cn, todvince@mail.ustc.edu.cn, or zcz@ustc.edu.cn.

This article contains supporting information online at http://www.pnas.org/lookup/suppl/doi:10.1073/pnas.2118656119/-/DCSupplemental.

Published March 29, 2022.

some P4A ATPases, such as ATP8B1 and ATP8B2, are able to form complexes with either CDC50A or CDC50B (14, 15). Recently, a series of structures of human P4A ATPases (ATP8A1 and ATP11C) complexed with CDC50A have been reported (16–18). However, the complex structure of P4A ATPase with CDC50B remains unknown.

ATP8B1, a member of P4 ATPase, is also known as FIC1 (familial intrahepatic cholestasis type 1) (19). It colocalizes with the primary bile-salt export pump ABCB11 in cholangiocytes and the canalicular membrane of hepatocytes (20). To counteract the disturbance of the asymmetric homeostasis of the cell membrane resulting from lipid flow accompanied by bile-acid transport driven by ABCB11 (21), the floppase ABCB4 exports PC to envelop bile-acid micelles (22), and ATP8B1 flips PS (23) or PC (24) from the outer to the inner membrane leaflet to restore membrane asymmetry. Defects in ATP8B1 are usually associated with severe human diseases, such as the intrahepatic cholestasis diseases PFIC1 (progressive FIC1) and BRIC1 (benign recurrent intrahepatic cholestasis type 1) (25).

Here, we solved the cryo-electron microscopy (cryo-EM) structures of apo-form ATP8B1–CDC50A and ATP8B1–CDC50B and a PS-bound structure of ATP8B1–CDC50A. These structures unraveled a yet-unknown autoinhibited phosphorylated state of P4 ATPases, which is activated upon substrate binding. These findings not only advance our understanding of the molecular mechanism of P4 ATPases, but also provide a structural platform for further therapeutic intervention of intrahepatic cholestasis diseases.

Results

The ATPase Activities of ATP8B1–CDC50A/B Are Significantly Stimulated by PS. We overexpressed human ATP8B1–CDC50A and ATP8B1–CDC50B in HEK293F cells, with a Flag tag fused to the N terminus of ATP8B1, and purified the complexes using an affinity column followed by size-exclusion chromatography (SEC). Sodium dodecyl sulfate (SDS)-polyacrylamide gel electrophoresis indicated that both complexes were purified in a homogeneous state (*SI Appendix*, Fig. S1). As substrates were reported to greatly enhance the ATPase activity of P4 ATPases (16, 18, 26), we performed ATPase activity in the presence or absence of different phospholipids at the concentration of 300 μM. Dodecyl-β-D-maltopyranoside (DDM; 1%, weight [wt]/volume [vol]) was added as the hydrotropic agent for the dissolution of lipids to produce clear and homogeneous stock solutions at room temperature. The ATPase activities of both ATP8B1–CDC50A and ATP8B1–CDC50B showed a significant increase when PS was added compared with the basal activity (Fig. 1*A*). The EC_{50} (concentration for 50% of maximal effect) values of PS-dependent ATPase activities for the ATP8B1–CDC50A and ATP8B1–CDC50B complexes were 63.6 ± 3.8 and 87.1 ± 3.7 μM, with V_{max} values of 269.1 ± 8.0 and 244.4 ± 3.7 $nmol{\cdot}min^{-1}{\cdot}mg^{-1}$, respectively (Fig. 1*B*). However, PC only showed a modest stimulation of the ATPase activity for ATP8B1–CDC50B, but no significant effect for ATP8B1–CDC50A. In contrast, PE had no effect on ATPase activity stimulation for both complexes. Considering that the phase properties of the PS, PC, and PE lipids are quite different, we further performed ATPase activity assays in the proteoliposomes to compare the activities upon the addition of extra PS, PC, or PE with the activity assay system in PC. ATP8B1–CDC50A/B were reconstituted in 100% PC; 90% PC and 10% PS; and 90% PC and 10% PE, respectively, and showed similar activities to those in the detergents (*SI Appendix*, Fig. S2). We also performed the phospholipid flippase activity assays using a dithionite-based quenching approach in proteoliposomes (27). The PS and PC analogs bearing a fluorescent 7-nitro-2-1,3-benzoxadiazol-4-yl (NBD) group were used as the substrates, and the assays displayed a weak, but obvious, flippase activity of ATP8B1–CDC50A/B complex toward NBD-PS (Fig. 1*C* and *SI Appendix*, Fig. S3). In contrast, the activity toward NBD-PC was not detectable. These results revealed that PS is the most favored substrate of ATP8B1–CDC50A/B.

Bile Acids Can Further Augment the ATPase Activity. It is puzzling that the V_{max} of ATP8B1 is less than 1/6 of the previously reported P4 ATPases (16, 18, 26). Notably, the yeast P4 ATPase Drs2p in complex with Cdc50p with a nondetectable ATPase activity in the presence of substrate could be activated by an activator molecule, lipid phosphatidylinositol 4-phosphate (PI4P) (28). In addition, bile acids could enhance the ATPase activities of ABCB4 (29) and ABCG5/G8 (30), both of which are localized in hepatocytes like ATP8B1. Thus, we tested the ATPase activities of ATP8B1–CDC50A/B complexes in the presence of cholate, the main component of bile acids. However, the addition of cholate alone only exhibited a slight increase in activity for both complexes, compared with the basal activity (Fig. 1*D*). Compared with the activities of ATP8B1–CDC50A/B in the presence of PS solubilized in the detergent DDM at ∼230 or 180 $nmol{\cdot}min^{-1}{\cdot}mg^{-1}$, the two complexes in the presence of PS solubilized in cholate displayed a significantly increased activity to ∼2 or 3 $\mu mol{\cdot}min^{-1}{\cdot}mg^{-1}$ (Fig. 1*D*). Notably, the ATPase activity of ATP8B1 in the presence of 300 μM cholate and 100 μM PS is comparable to that of other characterized P4 ATPases (16, 18, 26, 31). We introduced a mutation (E234Q) in the DGET motif of the A domain that prevents the dephosphorylation of the phosphorylated ATP8B1, and the mutant displayed a significant decrease of activity compared with the wild type (Fig. 1*D*). The activity could also be completely inhibited by AlF_4^-, an inhibitor of P-type ATPases (32). The ATPase activity assays in the presence of PS solubilized in other detergents, such as octyl glucoside and glyco-diogenin (GDN), yielded an activity similar to that in DDM (*SI Appendix*, Fig. S4*A*). Cholate concentration-dependent stimulated ATPase activities in the presence of 50 μM PS solubilized in DDM further suggested that the bile salt could serve as an activator (*SI Appendix*, Fig. S4*B*). Moreover, PS solubilized in either primary or secondary conjugated bile acids could greatly augment the ATPase activity (Fig. 1*E*), compared with that in DDM. Notably, tauro-conjugated bile acids, including taurocholic acid (TC), have higher augmentation rates. All these data suggested that various bile acids can augment the PS-simulated ATPase activity of ATP8B1–CDC50A/B.

Overall Structures of ATP8B1–CDC50A and ATP8B1–CDC50B. We solved the 3.4-Å cryo-EM structures of the ATP8B1–CDC50A and ATP8B1–CDC50B complexes, respectively (Fig. 2 *A* and *B*), which followed the gold-standard Fourier shell correlation criterion of 0.143 (*SI Appendix*, Table S1 and Figs. S5 and S6). About 95% of the complete sequence could be modeled in both structures, except for a few disordered regions, most at the termini (Met1∼Glu13, Glu30∼Lys60, and Arg1228∼Ser1251 of ATP8B1; Met1∼Ala23 and Asn355∼Ile361 of CDC50A; and Met1∼Ala7 and Asp346∼Glu351 of CDC50B). Superposition of the two complex structures yields an rmsd of 0.42 Å over 990 Cα atoms, indicating that the two structures resemble each other. Similar to the previously reported P4 ATPase structures, ATP8B1 also has a TM domain of 10 TMs (TM1–10) and three cytoplasmic domains: the A

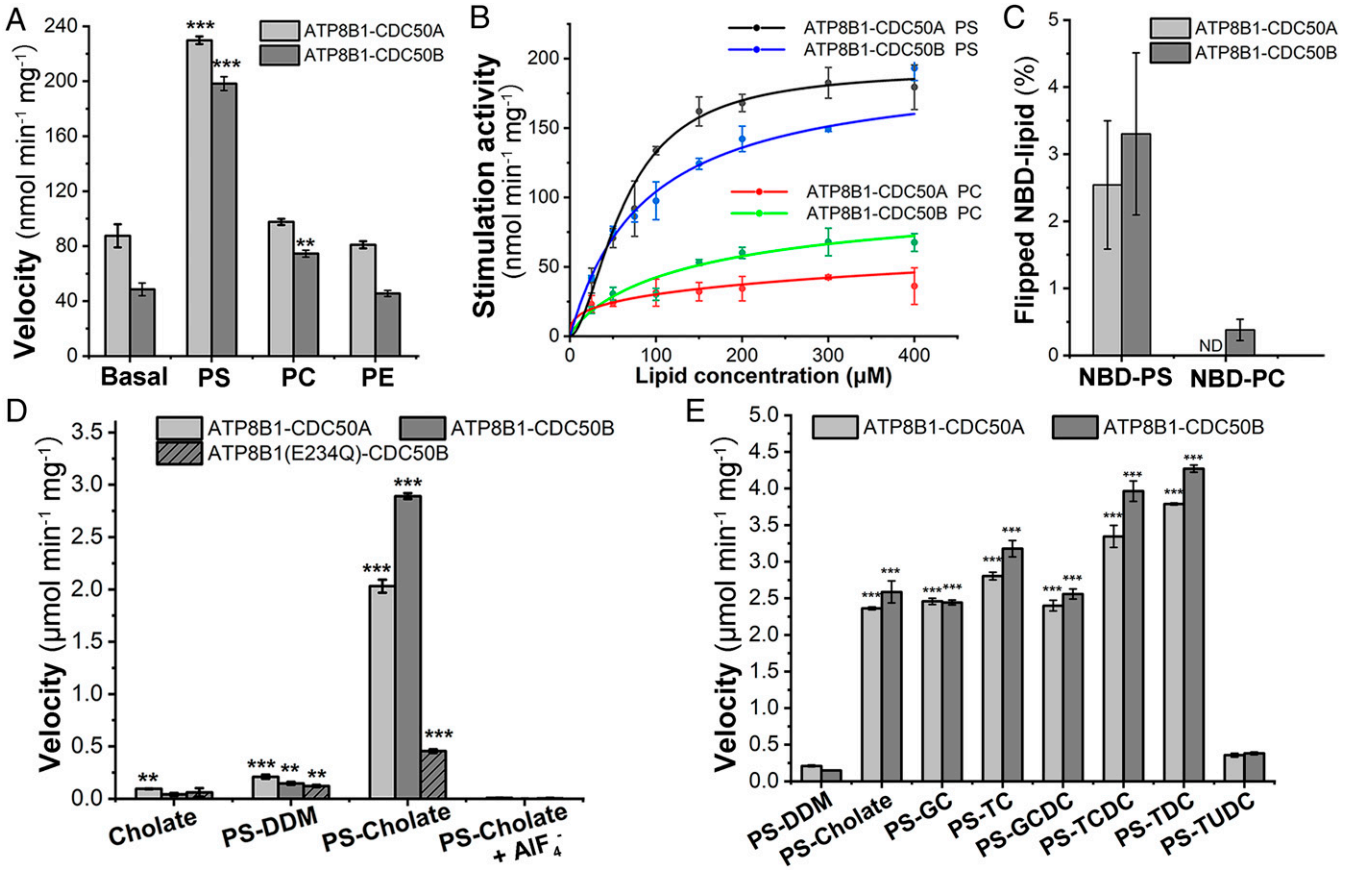

Fig. 1. Substrate-stimulated and bile-acid-augmented ATPase activity assays of ATP8B1–CDC50A and ATP8B1–CDC50B complexes. (*A*) ATPase activities of ATP8B1–CDC50A/B in different phospholipids. The final concentration of the phospholipids was set to 300 μM dissolved in 0.03% (wt/vol) DDM. (*B*) The phospholipid concentration-dependent ATPase activities of ATP8B1–CDC50A/B. Data points represent the means ± SD of three measurements at 37 °C and were fitted by the Hill equation. (*C*) Flippase activity assays shown as the percentages of flipped NBD-lipids. ND, nondetected. (*D*) Cholate-augmented ATPase activities of ATP8B1–CDC50A/B in the presence of PS. The PS was dissolved in DDM or cholate sodium, and a final concentration of PS was set to 100 μM dissolved in 0.01% (wt/vol) DDM or 300 μM cholate sodium. AlF_4^- was produced by mixing 2 mM $AlCl_3$ and 10 mM NaF. (*E*) Augmented ATPase activity of ATP8B1–CDC50A/B upon addition of PS dissolved in various bile acids (final concentration: 100 μM PS dissolved in 300 μM various bile acids). GC, glycocholic acid; TCDC, taurochenodoxycholic acid; GCDC, glycochenodeoxycholic acid; TDC, taurodeoxycholic acid; TUDC, tauroursodeoxycholate acid. At least three independent assays were performed to calculate the means and SDs, and the data are presented as the means ± SD. Two-tailed Student's *t* test was used for the comparison of statistical significance. $^{**}P < 0.01$; $^{***}P < 0.001$.

(actuator), N (nucleotide-binding), and P (phosphorylation) domains (Fig. 2 *A* and *B*). The N domain is responsible for binding to ATP, which donates the phosphate group for autophosphorylation of the conserved Asp454 of the P domain, generating a phosphorylated intermediate during the transport cycle. The A domain can dephosphorylate the phosphorylated P domain via the catalytic residue Glu234 and, finally, triggers substrate translocation. In addition, the N terminus and C terminus form long loops, termed the N-tail and C-tail, respectively, which might function as regulatory domains (33). In both complexes, superposition of CDC50A and CDC50B gives a quite similar structure with an rmsd of 0.79 Å over 269 Cα atoms, in agreement with their high sequence identity of 54% (*SI Appendix*, Fig. S7). CDC50A/B interact with ATP8B1 through the extracellular domains, the two TMs and an unstructured loop preceding the N terminus of the TMs, forming three interfaces almost identical in the two complexes. These interfaces are conserved in known structures of P4 ATPases complexed with CDC50A (16, 17).

ATP8B1 Adopts an Autoinhibited E2P State. The transport cycle of P4 ATPases has been clearly depicted by the Post–Albers scheme (34, 35), including several intermediate states (*SI Appendix*, Fig. S8): ATP binding (E1-ATP), phosphorylated (E1P and E2P), substrate binding (E2Pi-PL), dephosphorylated (E2), and substrate release (E1) states (8). These states have been captured in a previous report of the cryo-EM structure of ATP8A1–CDC50A (16). Superposition of ATP8B1 with the known structures of ATP8A1 revealed that ATP8B1 possesses a lowest rmsd of 2.01 Å with ATP8A1 in the E2P state (Fig. 2*C* and *SI Appendix*, Fig. S9).

In our two structures, an extra density could be found in proximity to residue Asp454 from the conserved DKTG motif of the P domain, which could be fitted with a PO_4^- and a Mg^{2+} ion (Fig. 2*D*), indicating that Asp454 is phosphorylated. The Mg^{2+} ion is coordinated by Asp454, Thr456, Asp893, and PO_4^- (Fig. 2*D*). However, the catalytic residue Glu234 from the conserved DGET motif of the A domain is stabilized by Asp232, Lys238, and Arg867 via salt bridges and hydrogen bonds (H-bonds). As a result, the phosphorylated Asp454 is too far away from Glu234 to be dephosphorylated, which is a feature of the E2P state (16). Thus, ATP8B1 is most likely in the E2P state, in which the P domain has been phosphorylated and ready to bind the substrate.

Superposition of ATP8B1 against ATP8A1, both at the E2P state, revealed that the core structures can be well superimposed

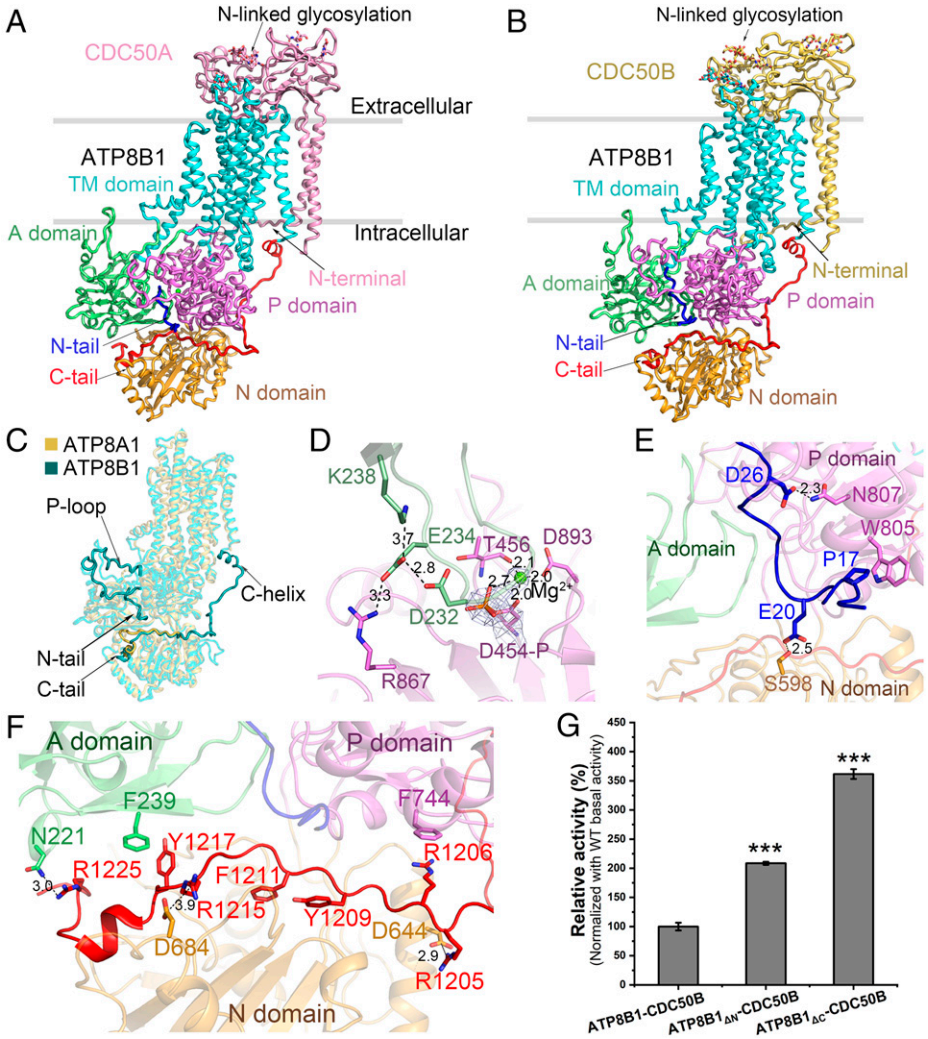

Fig. 2. Structures of ATP8B1–CDC50A and ATP8B1–CDC50B at the autoinhibited phosphorylated state. Overall structures of ATP8B1–CDC50A (*A*) and ATP8B1–CDC50B (*B*) are shown as cartoons. The major domains and motifs are labeled in different colors. The same color scheme is used throughout the manuscript. (*C*) Structure superposition of ATP8B1–E2P against ATP8A1–E2P (PDB ID code: 6K7L). ATP8B1 and ATP8A1 are colored in cyan and yellow-orange, respectively. (*D*) The phosphorylation site of ATP8B1. The phosphorylated Asp454 from the P domain and related residues are shown as sticks. PO_4^- is shown as sticks, and Mg^{2+} is shown as spheres. Densities are shown as gray mesh, contoured at 8σ. Interactions of the N-tail (*E*) and the C-tail (*F*) with the cytoplasmic domains. All interacting residues are shown as sticks. (*G*) ATPase activities of the N-tail or C-tail truncated ATP8B1 in complex with CDC50B compared with the wild type. Δ*N* and Δ*C* stand for the deletion of N-terminal Met1~Glu30 and C-terminal Ala1187~Ser1251, respectively. Data were normalized against the basal activity of ATP8B1–CDC50B. At least three independent assays were performed to calculate the means and SDs, and the data are presented as the means ± SD. Two-tailed Student's *t* test was used for the comparison of statistical significance. ***$P < 0.001$. Structures of ATP8B1 shown in *C*–*F* are derived from the complex structure of ATP8B1–CDC50B.

(Fig. 2*C*). However, both the N-tail and C-tail insert into the clefts of the three cytoplasmic domains of our ATP8B1 (Fig. 2 *A* and *B*), whereas the N terminus of ATP8A1 is missing in their structure (Fig. 2*C*) (16). Specifically, the N-tail interacts with the P domain by H-bonds (Asp26–Asn807) and hydrophobic interactions between Pro17 and Trp805 and interacts with the N domain via an H-bond between Glu20–Ser598 (Fig. 2*E*). The C-tail interacts with the P domain via the cation–π interaction between Arg1206 and Phe744, the A domain via a π–π interaction between Phe239–Tyr1217 and an H-bond between Asn221–Arg1225, and the N domain via two pairs of salt bridges between Asp644–Arg1205 and Asp684–Arg1215 (Fig. 2*F*). Remarkably, Tyr1209 and Phe1211 from the conserved GYAFS motif occupies the ATP binding site (Fig. 2*F*). Truncation of either the N-tail or C-tail of ATP8B1 resulted in an increased ATPase activity of approximately twofold or threefold to that of the wild type, respectively (Fig. 2*G*), further suggesting that ATP8B1 basically adopts an autoinhibited E2P state. Besides ATP8A1, an autoinhibited state of yeast Drs2p have been reported, which was also inhibited by the C-terminal tail only (36, 37). In addition, an N-terminal inhibited state of yeast P5B ATPase Ypk9 was reported (9). In the structure, the N terminus of Ypk9 resides between the N, A, and P domains (*SI Appendix*, Fig. S10), which partly resembles our case of ATP8B1. It is notable that all of these previously reported autoinhibited structures at the E2P state were obtained upon the addition of the phosphate analog beryllium fluoride (BeF_3^-), which differs from our autoinhibited structure of ATP8B1 in the absence of any additives.

The Positively Charged P-Loop Is Responsible for the Recruitment of Bile Acids. Superposition of ATP8B1 against ATP8A1 also revealed an extra loop in ATP8B1 protruding from the P domain (hence, named the P-loop) (Fig. 2*C*), which is rich in positively charged residues. Further structural analysis revealed two other positively charged segments from the C-tail, which

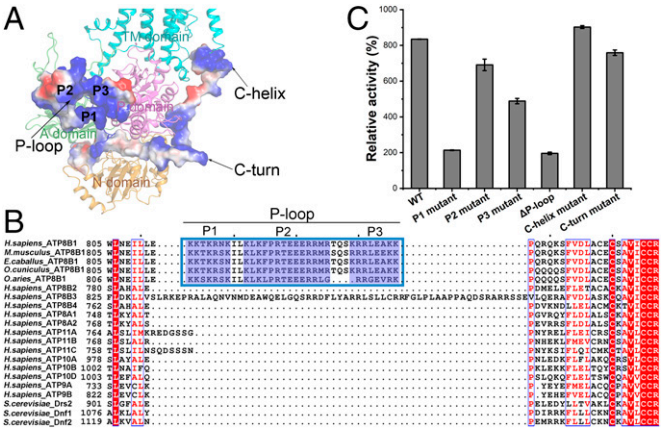

Fig. 3. The P-loop conserved in ATP8B1 and orthologs is essential for the recruitment of bile acids. (*A*) The three positively charged regions of ATP8B1, namely, the P-loop, C-helix, and C-turn. The positively charged residues on the P-loop were grouped into three clusters as P1, P2, and P3. (*B*) Multiple-sequence alignment of the P-loop and flanking regions in P4-type ATPases. The P-loops rich in positively charged residues in ATP8B1 and orthologs are marked with a blue box. (*C*) Relative ATPase activities of ATP8B1–CDC50B and mutants in the presence of 100 μM PS dissolved in 300 μM TC, with the corresponding activity in the presence of PS dissolved in DDM setting as 100%. At least three independent assays were performed to calculate the means and SDs, and the data are presented as the means ± SD. WT, wild type.

are termed the C-helix (residues Ser1172–Arg1184) and the C-turn (residues Arg1193–Arg1206), respectively (Fig. 3*A*). There are 16 positively charged residues in the 34-residue P-loop of ATP8B1, which is absent in other P4-type ATPases (Fig. 3*B* and *SI Appendix*, Fig. S11). The C-helix is a short helix corresponding to the amphipathic helix of yeast Drs2p, which is adjacent to the binding site of the activator PI4P (36), while the C-turn is an arginine-rich sharp turn of the C-tail (*SI Appendix*, Fig. S11*A*). Considering that bile acids are negatively charged under physiological conditions (38), the three segments might be responsible for the recruitment of bile acids.

Hence, we truncated the P-loop (residues from Lys813 to Lys846) and mutated the positively charged residues in the C-helix (K1177E–K1180E–H1181D–R1182E–K1183E–R1184E–K1186E) and C-turn (R1194T–R1199S–R1200S–R1206S) for ATPase activity assays. The results showed that the truncation of the P-loop led to a significant reduction in TC-augmented activity compared with the wild type, whereas either the C-helix or C-turn mutant displayed no obvious change in activity (Fig. 3*C*). It suggested that the P-loop, which is conserved in ATP8B1 orthologs according to the multisequence alignment (Fig. 3*B*), might be responsible for the recruitment of bile acids.

We grouped the positively charged residues on the P-loop into three clusters as P1, P2, and P3 (Fig. 3*B*) and constructed three mutants with these residues in each cluster mutated to glycine and/or serine, respectively (P1 mutant: K813G–K814S–K816G–R817S–K819S; P2 mutant: K822S–K824S–R827G–R832G–R833S–R835G; and P3 mutant: K839G–R840S–R841G–K845S–K846S), for the bile-acid-augmented ATP hydrolysis assays. It indicated that only the positively charged residues in P1 might be involved in the recruitment of bile acid (Fig. 3*C*). Moreover, we performed a simulation of the TC molecule binding to the P-loop and found that the negatively charged taurine moiety of TC interacts with P1 of the P-loop (*SI Appendix*, Fig. S11), in agreement with the mutant activity assays. Thus, we propose that the P1 region, which is adjacent to the N-tail, might play the key role in bile-acid recruitment. In this simulation model, upon TC binding, the P-loop undergoes a conformational change of departure from the N-tail, presumably in consequence facilitating the release of the N-tail, which is rich in negatively charged residues ($_{14}$DSQPNDEVVPYSD-DE$_{29}$T), in the autoinhibition state.

The Substrate-Bound ATP8B1–CDC50A Structure Revealed the Release of Autoinhibition. To further investigate the substrate specificity of ATP8B1, we solved the cryo-EM structure of substrate-bound ATP8B1–CDC50A at a 4.0-Å resolution with the addition of PS and AlF_4^- (*SI Appendix*, Fig. S12). An extra density in the cavity formed by TM2, TM4, and TM6 of ATP8B1 could be fitted with a molecule of PS (Fig. 4*A*). The serine group of PS is stabilized by Thr143, Thr144, and Asn397, which are conserved in PS flippases (*SI Appendix*, Fig. S13). The phosphate group and glycerol backbone of PS are embraced by Ser403, Asn989, and Ser994 (Fig. 4*B*), which are conserved residues in most P4 ATPases (*SI Appendix*, Fig. S13). Notably, previous reports showed that clinical variants of S403Y and S994R of ATP8B1 were associated with the severe intrahepatic cholestasis disease PFIC1 (39, 40). Moreover, single mutation (T143A, T144A, N397Q, N397A, S403Y, N989A, or S994R) of the PS binding residues showed a significantly reduced ATPase activity in the presence of PS dissolved in TC (Fig. 4*C*). Notably, multiple-sequence alignment indicated that Asn397 in ATP8B1 differs from the conserved the glutamine residue on TM4 of PC transporters (*SI Appendix*, Fig. S13). Indeed, the N397Q mutant of ATP8B1 showed a significant decreased activity toward PS compared with wild type.

Remarkably, both the N-tail and C-tail of ATP8B1 are invisible in the PS-bound structure (Fig. 4*A*), suggesting the release of autoinhibition upon substrate binding. Superposition of this PS-bound structure against the apo-form ATP8B1 revealed significant rotations of TM1 and TM2 for ~10° and ~13°, respectively. In consequence, the cavity formed by TM2, 4, and 6 is closed by the TM1–2 loop in the outer leaflet and

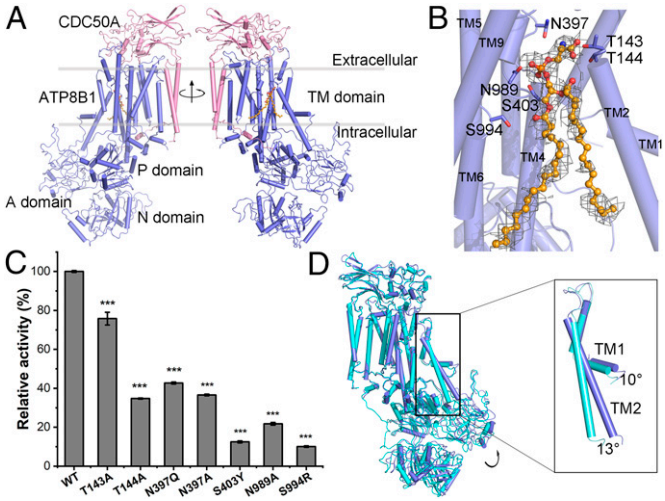

Fig. 4. The PS-bound structure of ATP8B1–CDC50A and the PS-binding site. (*A*) Overall structure of PS-bound ATP8B1–CDC50A. ATP8B1 is colored in slate; PS is shown as sticks and spheres in orange. (*B*) The PS-binding site. The density of the PS is shown in gray mesh, contoured at 3σ. (*C*) ATPase activities of ATP8B1–CDC50B mutants compared with the wild type (WT), in the presence of 100 μM PS dissolved in TC. Data were normalized against the activity of the wild type. At least three independent assays were performed to calculate the means and SDs, and the data are presented as the means ± SD. Two-tailed Student's *t* test is used for the comparison of statistical significance. ***$P < 0.001$. (*D*) Superposition of the autoinhibited E2P state against the PS-bound state of ATP8B1–CDC50A by aligning the TM7-10 of ATP8B1. The E2P state and PS-bound ATP8B1–CDC50A are colored in cyan and slate, respectively.

opened in the inner leaflet, a conformational change necessary for the release of lipid to the inner leaflet of the membrane. Furthermore, the rotation of TM1 and TM2 makes the A domain shift toward the P domain, which is subject to being dephosphorylated (Fig. 4*D*). This conformation is similar to that of ATP8A1 in the E2Pi-PL state (16), in which AlF_4^- substituted PO_4^- in proximity to residue Asp454 of the P domain; despite this, we could not fit AlF_4^- in our PS-bound structure due to the relatively low resolution of cytoplasmic domains (*SI Appendix*, Fig. S12). Superposition of the E2Pi-PL state ATP8B1 against the E2Pi-PL state ATP8A1 yielded an rmsd of 2.2 Å (*SI Appendix*, Fig. S14), and, moreover, PS in both structures could be well superimposed, including residues that were suggested to be a central hydrophobic gate for the lipid translocation, indicating that E2Pi-PL state ATP8B1 is also in the occluded state as ATP8A1 (16).

Discussion

An autoinhibited state has been reported in the previous structures of yeast Drs2p, the C-tail of which was found to lock the cytoplasmic domains (36, 37), similar to the inhibited E2P state of human ATP8A1 upon the addition of the inhibitor BeF_3^- (16). In addition, a recent report revealed a resting state of the yeast P5B ATPase Ypk9 autoinhibited by the N terminus (9). Our present structures, in complex with either CD50A or CDC50B, showed that ATP8B1 adopts an autoinhibited E2P state, in which the N-tail and C-tail separately insert into the cytoplasmic interdomain clefts, and the residue Asp454 of the P domain is phosphorylated. ATPase activity assays indicated that the activity of ATP8B1 could be inhibited by its own N-tail and C-tail, which might interrupt the interdomain cross-talk. Most likely, an inhibited E2P state for inhibiting the activity of P4 ATPases is necessary for the homeostasis of membrane lipid asymmetry.

Based on our findings and previous reports, we proposed a transport mechanism of ATP8B1 with an extra autoinhibited E2P state, which is an equilibrium state with the E2P state in the Post–Albers cycle of P4 ATPase (Fig. 5). As shown in our PS-bound structure, this autoinhibition state could be switched

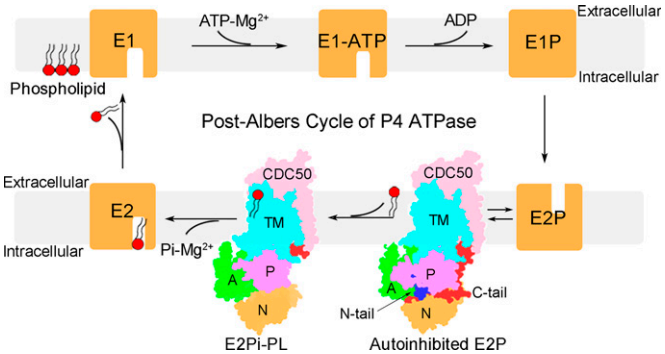

Fig. 5. Proposed transport mechanism. The two structures (autoinhibited E2P and E2Pi-PL state ATP8B1–CDC50A) we report here are shown as the schemes, with the domains of ATP8B1–CDC50 shown in different colors, whereas the rest states are shown as yellow squares. Binding and hydrolyzing ATP would trigger transition of ATP8B1 from the state E1 to E1P. Afterward, the rearrangement of the cytoplasmic domains makes ATP8B1 to adopt an E2P state, which is most likely equilibrated at the autoinhibited E2P state with the N-tail and C-tail inserting into the cytoplasmic interdomain clefts. The release of autoinhibition could be induced upon phospholipid binding and further accelerated in the presence of bile acids, switching ATP8B1 at the E2Pi-PL state. The ATP8B1 at the E2 state with a dephosphorylated P domain undergoes domain rearrangement accompanying with the release of phospholipid, and, finally, ATP8B1 returns to the E1 state.

to the E2Pi-PL state upon substrate binding (Fig. 5). In addition, our biochemical results indicated that bile acids can augment the PS-stimulated ATPase activity of ATP8B1, similar to the previous reports that PI4P can stimulate the ATPase activity of yeast Drs2p (28). Furthermore, mutations of the positively charged P-loop, which is highly conserved in ATP8B1 orthologs, led to a reduced ATPase activity of ATP8B1 in response to the addition of bile acids. In fact, ATP8B1 usually functions under a physiological environment with enriched bile acids; thus, the release of autoinhibition could be induced by the substrate and further accelerated upon the easily recruited bile acids.

A recent preprint paper also reported the apo-form structure of the ATP8B1–CDC50A complex, which displayed a similar autoinhibited state locked by both the N- and C-tails (41). In contrast, they discovered that PC could stimulate ATPase activity of ATP8B1 after the truncation of the N- and C-tails and activated by the addition of phosphoinositides. This discrepancy to our PS-stimulated activity assays may imply that ATP8B1 might adopt various regulatory mechanisms to flip different lipids.

In summary, ATP8B1 free of substrate basically adopts an autoinhibited conformation at the homeostatic membrane asymmetry. Once this asymmetry is altered, usually due to the phospholipid flow accompanying the efflux of bile acids across the membrane, ATP8B1 is fully activated in the presence of both substrate and bile acids. The present structural analysis together with biochemical assays supplement our understanding on the Post–Albers cycle of P4 ATPases.

Materials and Methods

Cloning and Expression. The full-length human *ATP8B1* (Uniprot: O43520), *CDC50A* (Uniprot: Q9NV96), and *CDC50B* (Uniprot: Q3MIR4) genes were synthesized after codon optimization for the mammalian cell-expression system by Sangon Biotech Company. The wild-type *ATP8B1* and mutants were subcloned into a pCAG vector with an N-terminal Flag-tag (DYKDDDDK). *CDC50A* and *CDC50B* were, respectively, subcloned into the same vector with a C-terminal 6×His-tag or an N-terminal 6×His-tag using the One Step Cloning Kit (Vazyme).

For protein expression, HEK293F cells were cultured in SMM 293T-II medium (Sino Biological, Inc.) at 37 °C with 5% CO_2. Cells were transfected when the density reached ~2.5 × 10^6 cells per mL. For transfection, ~1.8 mg of pCAG-ATP8B1 and ~0.3 mg of pCAG-CDC50A/B were incubated with 4 mg of linear polyethyleneimines (Polysciences, Inc.) in 45 mL of fresh medium for 15 min, followed by a 15-min static incubation. The transfected cells were grown at 37 °C with 5% CO_2 for 48 h before harvesting. Cell pellets were resuspended in the lysis buffer containing 50 mM Tris·HCl (pH 7.5), 150 mM NaCl, and 20% glycerol (vol/vol) after centrifugation at 1,500 × *g* for 10 min. The suspension was frozen in liquid nitrogen and stored at −80 °C for further use.

All mutants were generated with a standard PCR-based strategy and were cloned, overexpressed, and purified the same way as the wild-type protein.

Protein Preparation. For protein purification, 2 mM ATP (Sangon Biotech) and 2 mM $MgCl_2$ were added to the thawed suspension, and the mixture was incubated with additional 1% (wt/vol) DDM (Bluepus) and 0.2% (wt/vol) cholesteryl hemisuccinate (Anatrace) at 8 °C for 2 h for membrane solubilization and protein extraction. After ultracentrifugation at 45,000 rpm for 45 min (Beckman Type 70 Ti), the supernatant was incubated with the anti-Flag M2 affinity gel (Sigma) on ice for at least 40 min. Then, the resin was washed by 30 mL of wash buffer containing 50 mM Tris·HCl (pH 7.5), 150 mM NaCl, and 10% (vol/vol) glycerol, with 0.02% GDN (wt/vol; Anatrace) for ATP8B1–CDC50A or 0.06% digitonin (wt/vol; Apollo Scientific) for ATP8B1–CDC50B. The protein was eluted with 6 mL of wash buffer plus 200 μg/mL Flag peptide. The samples were further concentrated and purified by SEC on a Superose 6 Increase 10/300 or Superdex 200 Increase 10/300 gel-filtration column (GE Healthcare), pre-equilibrated with SEC buffer (50 mM Tris·HCl, pH 7.5, 150 mM NaCl, and 0.02% GDN or 0.06%

digitonin). The purified samples were analyzed by SDS-gel electrophoresis with a commercial precast acrylamide gel (with a gradient from 4 to 20%). The peak fractions were collected, concentrated to 4 to 6 mg/mL, frozen in liquid nitrogen, and stored at −80 °C before use.

Lipid and Detergent/Lipid Mixture Preparations. Lipids (Avanti) were prepared in 20 mM Tris·HCl (pH 7.5) and 75 mM KCl to a final concentration of 10 mg/mL (∼12.5 mM) by sonicating in a water-bath sonicator at room temperature until forming a homogenous solution. Bile acids (sodium salts) were dissolved at a final concentration of 100 mM in water and mixed with lipid stocks in a mole ratio of 3:1. Then, 20% (wt/vol) DDM stocks were prepared in water and added to the lipids solution in a final concentration of 1%. All the mixtures were frozen in liquid nitrogen and thawed at room temperature three times, resulting in a clear and homogeneous solution at room temperature. Lipid stocks, bile acids, and lipid mixtures were stored at −20 °C before use.

ATPase Activity Assays. For the substrate-stimulated ATPase activity assay, 2 μg of purified proteins was preincubated at room temperature for 5 min with or without 600 μM lipids in 150 μL of reaction buffer, containing 20 mM Tris·HCl (pH 7.5), 75 mM KCl, 2 mM $MgCl_2$, and 0.02% DDM. The proteins or protein/lipid mixtures were cooled in ice and further mixed with an equal volume of precooled reaction buffer containing 4 mM ATP. Reactions were performed at 37 °C for 20 min, and the amount of released phosphate group (Pi) was quantitatively measured by using the ATPase colorimetric Assay Kit (Innova Biosciences) in 96-well plates at $OD_{650\ nm}$.

The bile-acid-augmented assays were measured similarly to that mentioned above, except that the proteins were preincubated with detergent/lipids mixtures to a final lipid concentration of 200 μM dissolved in 600 μM bile acids.

Proteoliposome Preparation. Proteoliposomes were prepared by detergent removal using Bio-Beads SM-2 adsorption (42). All steps were performed at 4 °C, unless otherwise stated. Normally, lipid mixtures (99.5% brain polar lipids and 0.5% NBD–phospholipid) were resuspended in reconstitution buffer (20 mM Tris·HCl, pH 7.5, and 75 mM KCl) to the final concentration of 10 mg/mL The proteins were added to the destabilized liposomes (pretreated by 0.45% Triton X-100 for 1 h at room temperature) and incubated for 1 h. The ratio of lipids and proteins was kept at 80:1 (wt/wt). Triton X-100 was removed by incubation with SM-2 Adsorbent Bio-Beads (Bio-Rad) overnight and repeated for another 2 h. Then, 5 mM dithionite was added to the mixture to quench the free fluorescent lipid probes. Proteoliposomes were diluted and resuspended twice with the ice-cold reaction buffer by 250,000 × g for 1 h. The treated proteoliposomes were stored at 4 °C before use.

Flippase Activity Assays. Flippase activity was defined by a change of interleaflet distribution of fluorescent lipid probes (NBD–phospholipids) in proteoliposomes measured by using a dithionite-based quenching approach (27). For each individual measurement, 25 μL of proteoliposomes containing ∼100 ng of ATP8B1–CDC50A/B complexes were incubated with 4 mM ATP in the presence or absence of 8 mM $MgCl_2$ in 25 μL of reaction buffer (20 mM Tris·HCl, pH 7.5, and 75 mM KCl) at 37 °C. After 10 min of incubation, each sample was diluted to 100 μL and assayed for probe distribution. The fluorescence (F_T) was recorded continuously in a CLARIOstar fluorometer (BMG LABTECH, Inc.) (λ_{ex} = 485 nm, λ_{em} = 520 nm). After stable baseline was obtained (∼5 min), 10 μL of 50 mM dithionite dissolved in 1 M Tris·HCl (pH 10) was added to the sample and mixed to quench the fluorescent probes in the outer leaflet of liposomes, and fluorescence was recorded until a stable line was obtained (∼120 s, F_D). Subsequently, the sample was solubilized by the addition of 10 μL of 10% Triton X-100, and the background fluorescence (F_0) was recorded for another 180 s. The percentage of NBD–phospholipid in the outer leaflet of proteoliposomes that is accessible to dithionite quenching was calculated as $(F_T/F_D)/(F_T/F_0) \times 100\%$.

Cryo-EM Sample Preparation. For the apo-form ATP8B1–CDC50A or ATP8B1–CDC50B complex, purified proteins were concentrated to 4.5 mg/mL. After centrifugation at 14,000 × g for 10 min, 3.5-μL samples were placed on glow-discharged holey carbon grids (Quantifoil, Cu R1.2/1.3, 300-mesh) with blot force setting of −2 and blot time of 3 s and plunged into liquid ethane by using Vitrobot Mark IV (FEI) at 8 °C and 100% humidity.

For the substrate-bound sample, ATP8B1–CDC50A purified by the anti-Flag M2 affinity gel was preincubated with 2 mM $AlCl_3$, 10 mM NaF, and 2 mM $MgCl_2$ overnight. The mixture samples were further concentrated and purified by SEC. The purified ATP8B1–CDC50A was concentrated to 5 mg/mL and incubated with additional 1 mM $AlCl_3$, 5 mM NaF, 2 mM $MgCl_2$, and 10 μM 1,2-dioleoyl-*sn*-glycero-3-phospho-L-serine for 1 h in ice. The 3.5-μL samples were placed on glow-discharged holey carbon grids (Quantifoil, Cu R1.2/1.3, 300-mesh) with blot force setting of −2 and blot time of 3 s and plunged into liquid ethane by using Vitrobot Mark IV (FEI) at 8 °C and 100% humidity.

Cryo-EM Data Collection. The cryo-EM grids of apo-form ATP8B1–CDC50A were loaded into a Titan Krios transmission electron microscope (ThermoFisher Scientific) operated at 300 KeV with a Gatan K2 Summit direct electron detector at the Center for Integrative Imaging, University of Science and Technology of China (USTC). A total of 3,003 movie stacks were collected in super-resolution mode at nominal magnification of 29,000× with a defocus range from −2.5 to −1.5 μm. Each movie stack of 32 frames was exposed for 6.4 s under a dose rate of 10 e^-/pixel/s, resulting in a total dose of ∼60 e^- $Å^{-2}$.

The cryo-EM data of apo-form ATP8B1–CDC50B complex were collected at the Center for Biological Imaging at the Institute of Biophysics (IBP), Chinese Academy of Sciences (CAS). A total of 3,717 micrographs were collected in super-resolution mode with a K3 camera at nominal magnification of 22,500× with a defocus range from −1.5 to −2.0 μm. Exposures of 6.4 s fractionated into 32 frames were collected at a dose rate of 1.5 or 1.6 e^- $Å^{-2}$ per frame, corresponding to a total dose of ∼60 e^- $Å^{-2}$.

The cryo-EM data of PS-bound ATP8B1–CDC50A were collected at 300 KeV with a Gatan K2 Summit direct electron detector at the Center for Integrative Imaging of USTC. A total of 2,983 movie stacks were collected in super-resolution mode at nominal magnification of 29,000× with a defocus range from −2.5 to −1.5 μm. Each movie stack of 32 frames was exposed for 6.4 s under a dose rate of 10 e^-/pixel/s, resulting in a total dose of ∼60 e^- $Å^{-2}$.

Cryo-EM Data Processing. All movie frames were corrected for gain reference and binned by a factor of 2 to yield a pixel size of 1.06 Å in RELION3.1 (43) through MotionCor2 (44). The contrast transfer function (CTF) parameters were estimated from the corrected movie frames using CTFFIND4 (45). After manual inspection of the micrographs, ∼3,000 particles were manually selected. Particles were automatically extracted by RELION with binning factor 2.

For apo-form ATP8B1–CDC50A, a total of 773,161 particles were picked and subjected to two-dimensional (2D) classification. After multirounds of 2D classification, 399,091 particles were selected for further three-dimensional (3D) classification with three classes using the reference generated by the 3D initial model. A total of 182,618 particles from the best class were refined and re-extracted for further 3D refinement. To improve the EM density, 3D skip alignment classification, followed by CTF refinement and Bayesian polishing, were performed, giving rise to an average resolution of 3.4 Å.

For apo-form ATP8B1–CDC50B, 2,561,714 particles were automatically extracted and subjected to 2D classification. A total of 494,609 particles were selected for further 3D classification with four classes using the reference generated by the 3D initial model. A total of 160,435 particles from one of the classes were further refined and postprocessed to yield a 3.4-Å map.

For PS-bound ATP8B1–CDC50A, 1,286,936 particles were automatically extracted and subjected to 2D classification. A total of 230,809 particles were selected for further 3D classification with three classes using the reference generated by the 3D initial model. A total of 159,960 particles from the best class were refined and reextracted for further 3D refinement. The 3D skip alignment classification, followed by CTF refinement and Bayesian polishing, was performed, giving rise to an average resolution of 4.0 Å.

The data-processing pipelines are presented in *SI Appendix*. Map resolution was estimated with the gold-standard Fourier shell correlation 0.143 criterion (46). Local resolutions were estimated by using Resmap with RELION3.1 (43).

Model Building and Refinement. The final sharpened map with a B-factor of −140 $Å^2$ was used for model building in Coot (47). Initial structure models for ATP8B1 and CDC50B were predicted by SWISS-MODEL (48). The CDC50A structure was obtained from PDB 6K7L. The initial model of ATP8B1–CDC50A/B complexes were built by fitting the ATP8B1 and CDC50A/B model into the map using UCSF Chimera (49). Then model building and refinement were accomplished manually by Coot (47). After several rounds of manual building, the model was almost completely built and automatically refined against the map

by the real_space_refine program in PHENIX (50) with secondary structure and geometry restraints. Figures were prepared with Pymol (51) or Chimera (49).

Molecular Dynamics Simulations. The initial model of TC docking to ATP8B1 was prepared by using HADDOCK (52). Starting from the best cluster model, a molecular dynamics (MD) simulation was conducted on residues 803 to 858. The Amber20 software package (53) with the ff19SB force field was used. The Generation Amber Force Field was used to generate parameters of TC. A periodic boundary condition of truncated tetrahedral box was adopted. The minimum distance from the solute to the boundary was 10 Å. The box was filled with TIP3P (54) water molecules and nine Cl^- ions. To eliminate bad contacts, the whole protein was restrained (the force constant was 500 kcal·mol^{-1}·Å^{-2}), and the waters and ions were minimized to 2,000 steps by using the steepest decent method in the first 1,500 steps, followed by 500 steps conjugate gradient minimization. In the second stage of energy minimization, restraints on the protein were removed, except for residues 803 to 809 and 849 to 858 (force constant was 1 kcal·mol^{-1}·Å^{-2}). Again, 2,000 steps were performed, with the first 1,500 steps using the steepest descent method and the last 500 steps using the conjugate gradient algorithm. Then, during a constant volume MD of 100 ps, the system was heated from 0 to 300 K, and the weak restraint to the solute was 10 kcal·mol^{-1}·Å^{-2}. After that, by setting skinnb to 5.0 Å, an equilibration simulation of 500 ps was performed under the isothermal-isobaric ensemble condition, with the whole protein restrained (force constant was 10 kcal·mol^{-1}·Å^{-2}). Finally, the Langevin dynamics with a collision frequency of 1.0 ps^{-1} was used to adjust the temperature, and the graphics processing unit accelerated pmemd.cuda code was used to conduct an MD simulation of 100 ns under the isothermal-isobaric ensemble condition, with the residues 803 to 809 and 849 to 858 weakly restrained (force constant was 10 kcal·mol^{-1}·Å^{-2}). The skinnb value was set to its default value of 2.0 Å. The 2-fs time step was used. All bonds, including hydrogen atoms, were restricted by using the SHAKE algorithm. Pressure was controlled at 1 bar by isotropic position scaling, and the relaxation time was 2.0 ps. For a limited range of nonbonded interactions, long-range electrostatic interaction was calculated by using the Particle-mesh Ewald method with a cutoff value of 10 Å.

Data Availability. All study data are included in the article and/or *SI Appendix*. Atomic coordinates and EM density maps of the autoinhibited E2P state ATP8B1–CDC50A (PDB: 7VGI; EMDB: EMD-31970), autoinhibited E2P state ATP8B1–CDC50B (PDB: 7VGH; EMDB: EMD-31969) and, PS-bound ATP8B1–CDC50A (PDB: 7VGJ; EMDB: EMD-31971) complexes in this paper have been deposited in the Protein Data Bank and the Electron Microscopy Data Bank, respectively.

ACKNOWLEDGMENTS. We thank Dr. Yongxiang Gao at the Center for Integrative Imaging, USTC; Xu-jing Li; and colleagues at the Center for Biological Imaging at the IBP, CAS for the cryo-EM image acquisition. This work was supported by the Ministry of Science and Technology of China (Grant ID: 2019YFA0508500), the Strategic Priority Research Program of the CAS (Grant ID: XDB37020202), and the National Natural Science Foundation of China (Grant ID: 91953101).

Author affiliations: [a]School of Life Sciences, Division of Life Sciences and Medicine, University of Science and Technology of China, Hefei 230027, China; [b]The First Affiliated Hospital of USTC, University of Science and Technology of China, Hefei 230027, China; [c]Biomedical Sciences and Health Laboratory of Anhui Province, University of Science and Technology of China, Hefei 230027, China; [d]School of Data Science, University of Science and Technology of China, Hefei 230026, China; and [e]Department of Physics, University of Science and Technology of China, Hefei 230026, China

1. P. A. Leventis, S. Grinstein, The distribution and function of phosphatidylserine in cellular membranes. *Annu. Rev. Biophys.* **39**, 407–427 (2010).
2. J. C. Holthuis, A. K. Menon, Lipid landscapes and pipelines in membrane homeostasis. *Nature* **510**, 48–57 (2014).
3. J. P. Andersen *et al.*, P4-ATPases as phospholipid flippases-structure, function, and enigmas. *Front. Physiol.* **7**, 275 (2016).
4. E. M. Bevers, P. L. Williamson, Getting to the outer leaflet: Physiology of phosphatidylserine exposure at the plasma membrane. *Physiol. Rev.* **96**, 605–645 (2016).
5. H. M. Hankins, R. D. Baldridge, P. Xu, T. R. Graham, Role of flippases, scramblases and transfer proteins in phosphatidylserine subcellular distribution. *Traffic* **16**, 35–47 (2015).
6. M. M. Babashamsi, S. Z. Koukhaloo, S. Halalkhor, A. Salimi, M. Babashamsi, ABCA1 and metabolic syndrome; a review of the ABCA1 role in HDL-VLDL production, insulin-glucose homeostasis, inflammation and obesity. *Diabetes Metab. Syndr.* **13**, 1529–1534 (2019).
7. M. Dyla, M. Kjærgaard, H. Poulsen, P. Nissen, Structure and mechanism of P-type ATPase ion pumps. *Annu. Rev. Biochem.* **89**, 583–603 (2020).
8. J. A. Lyons, M. Timcenko, T. Dieudonné, G. Lenoir, P. Nissen, P4-ATPases: How an old dog learnt new tricks–Structure and mechanism of lipid flippases. *Curr. Opin. Struct. Biol.* **63**, 65–73 (2020).
9. P. Li, K. Wang, N. Salustros, C. Grønberg, P. Gourdon, Structure and transport mechanism of P5B-ATPases. *Nat. Commun.* **12**, 3973 (2021).
10. M. J. McKenna *et al.*, The endoplasmic reticulum P5A-ATPase is a transmembrane helix dislocase. *Science* **369**, eabc5809 (2020).
11. M. Palmgren, J. T. Østerberg, S. J. Nintemann, L. R. Poulsen, R. L. López-Marqués, Evolution and a revised nomenclature of P4 ATPases, a eukaryotic family of lipid flippases. *Biochim. Biophys. Acta Biomembr.* **1861**, 1135–1151 (2019).
12. K. Segawa, S. Kurata, S. Nagata, The CDC50A extracellular domain is required for forming a functional complex with and chaperoning phospholipid flippases to the plasma membrane. *J. Biol. Chem.* **293**, 2172–2182 (2018).
13. Y. Katoh, M. Katoh, Identification and characterization of CDC50A, CDC50B and CDC50C genes in silico. *Oncol. Rep.* **12**, 939–943 (2004).
14. S. Bryde *et al.*, CDC50 proteins are critical components of the human class-1 P4-ATPase transport machinery. *J. Biol. Chem.* **285**, 40562–40572 (2010).
15. L. M. van der Velden *et al.*, Heteromeric interactions required for abundance and subcellular localization of human CDC50 proteins and class 1 P4-ATPases. *J. Biol. Chem.* **285**, 40088–40096 (2010).
16. M. Hiraizumi, K. Yamashita, T. Nishizawa, O. Nureki, Cryo-EM structures capture the transport cycle of the P4-ATPase flippase. *Science* **365**, 1149–1155 (2019).
17. H. Nakanishi *et al.*, Transport cycle of plasma membrane flippase ATP11C by cryo-EM. *Cell Rep.* **32**, 108208 (2020).
18. H. Nakanishi *et al.*, Crystal structure of a human plasma membrane phospholipid flippase. *J. Biol. Chem.* **295**, 10180–10194 (2020).
19. L. N. Bull *et al.*, A gene encoding a P-type ATPase mutated in two forms of hereditary cholestasis. *Nat. Genet.* **18**, 219–224 (1998).
20. E. F. Eppens *et al.*, FIC1, the protein affected in two forms of hereditary cholestasis, is localized in the cholangiocyte and the canalicular membrane of the hepatocyte. *J. Hepatol.* **35**, 436–443 (2001).
21. B. Stieger, The role of the sodium-taurocholate cotransporting polypeptide (NTCP) and of the bile salt export pump (BSEP) in physiology and pathophysiology of bile formation. *Handb. Exp. Pharmacol.* **201**, 205–259 (2011).
22. A. R. Crawford *et al.*, Hepatic secretion of phospholipid vesicles in the mouse critically depends on mdr2 or MDR3 P-glycoprotein expression. Visualization by electron microscopy. *J. Clin. Invest.* **100**, 2562–2567 (1997).
23. C. C. Paulusma *et al.*, ATP8B1 requires an accessory protein for endoplasmic reticulum exit and plasma membrane lipid flippase activity. *Hepatology* **47**, 268–278 (2008).
24. H. Takatsu *et al.*, Phospholipid flippase activities and substrate specificities of human type IV P-type ATPases localized to the plasma membrane. *J. Biol. Chem.* **289**, 33543–33556 (2014).
25. L. N. Bull, R. J. Thompson, Progressive familial intrahepatic cholestasis. *Clin. Liver Dis.* **22**, 657–669 (2018).
26. Y. He, J. Xu, X. Wu, L. Li, Structures of a P4-ATPase lipid flippase in lipid bilayers. *Protein Cell* **11**, 458–463 (2020).
27. J. C. McIntyre, R. G. Sleight, Fluorescence assay for phospholipid membrane asymmetry. *Biochemistry* **30**, 11819–11827 (1991).
28. X. Zhou, T. T. Sebastian, T. R. Graham, Auto-inhibition of Drs2p, a yeast phospholipid flippase, by its carboxyl-terminal tail. *J. Biol. Chem.* **288**, 31807–31815 (2013).
29. T. Kroll, S. H. J. Smits, L. Schmitt, Monomeric bile acids modulate the ATPase activity of detergent-solubilized ABCB4/MDR3. *J. Lipid Res.* **62**, 100087 (2021).
30. B. J. Johnson, J. Y. Lee, A. Pickert, I. L. Urbatsch, Bile acids stimulate ATP hydrolysis in the purified cholesterol transporter ABCG5/G8. *Biochemistry* **49**, 3403–3411 (2010).
31. J. Wang *et al.*, Proteomic analysis and functional characterization of P4-ATPase phospholipid flippases from murine tissues. *Sci. Rep.* **8**, 10795 (2018).
32. L. Bai *et al.*, Transport mechanism of P4 ATPase phosphatidylcholine flippases. *eLife* **9**, e62163 (2020).
33. M. G. Palmgren, P. Nissen, P-type ATPases. *Annu. Rev. Biophys.* **40**, 243–266 (2011).
34. R. W. Albers, Biochemical aspects of active transport. *Annu. Rev. Biochem.* **36**, 727–756 (1967).
35. R. L. Post, S. Kume, T. Tobin, B. Orcutt, A. K. Sen, Flexibility of an active center in sodium-plus-potassium adenosine triphosphatase. *J. Gen. Physiol.* **54**, 306–326 (1969).
36. M. Timcenko *et al.*, Structure and autoregulation of a P4-ATPase lipid flippase. *Nature* **571**, 366–370 (2019).
37. L. Bai *et al.*, Autoinhibition and activation mechanisms of the eukaryotic lipid flippase Drs2p-Cdc50p. *Nat. Commun.* **10**, 4142 (2019).
38. A. F. Hofmann, Bile acids: Trying to understand their chemistry and biology with the hope of helping patients. *Hepatology* **49**, 1403–1418 (2009).
39. A. Davit-Spraul *et al.*, ATP8B1 and ABCB11 analysis in 62 children with normal gamma-glutamyl transferase progressive familial intrahepatic cholestasis (PFIC): Phenotypic differences between PFIC1 and PFIC2 and natural history. *Hepatology* **51**, 1645–1655 (2010).
40. H. Egawa *et al.*, Intractable diarrhea after liver transplantation for Byler's disease: Successful treatment with bile adsorptive resin. *Liver Transpl.* **8**, 714–716 (2002).
41. T. Dieudonné *et al.*, Autoinhibition and regulation by phosphoinositides of ATP8B1, a human lipid flippase associated with intrahepatic cholestatic disorders. bioRxiv [Preprint] (2021). 10.1101/2021.11.03.467174 (4 November 2021).
42. S. N. Gummadi, S. Hrafnsdóttir, J. Walent, W. E. Watkins, A. K. Menon, Reconstitution and assay of biogenic membrane-derived phospholipid flippase activity in proteoliposomes. *Methods Mol. Biol.* **228**, 271–279 (2003).
43. S. H. W. Scheres, Amyloid structure determination in RELION-3.1. *Acta Crystallogr. D Struct. Biol.* **76**, 94–101 (2020).
44. S. Q. Zheng *et al.*, MotionCor2: Anisotropic correction of beam-induced motion for improved cryo-electron microscopy. *Nat. Methods* **14**, 331–332 (2017).
45. M. Su, goCTF: Geometrically optimized CTF determination for single-particle cryo-EM. *J. Struct. Biol.* **205**, 22–29 (2019).
46. P. B. Rosenthal, R. Henderson, Optimal determination of particle orientation, absolute hand, and contrast loss in single-particle electron cryomicroscopy. *J. Mol. Biol.* **333**, 721–745 (2003).

47. P. Emsley, B. Lohkamp, W. G. Scott, K. Cowtan, Features and development of Coot. *Acta Crystallogr. D Biol. Crystallogr.* **66**, 486–501 (2010).
48. A. Waterhouse *et al.*, SWISS-MODEL: Homology modelling of protein structures and complexes. *Nucleic Acids Res.* **46** (W1), W296–W303 (2018).
49. E. F. Pettersen *et al.*, UCSF Chimera–A visualization system for exploratory research and analysis. *J. Comput. Chem.* **25**, 1605–1612 (2004).
50. D. Liebschner *et al.*, Macromolecular structure determination using X-rays, neutrons and electrons: Recent developments in Phenix. *Acta Crystallogr. D Struct. Biol.* **75**, 861–877 (2019).
51. Schrodinger LLC, The PyMOL Molecular Graphics System, Version 1.8 (2015). https://pymol.org/2/. Accessed 18 March 2022.
52. R. V. Honorato *et al.*, Structural biology in the clouds: The WeNMR-EOSC ecosystem. *Front. Mol. Biosci.* **8**, 729513 (2021).
53. D. A. Pearlman *et al.*, Amber, a package of computer-programs for applying molecular mechanics, normal-mode analysis, molecular-dynamics and free-energy calculations to simulate the structural and energetic properties of molecules. *Comput. Phys. Commun.* **91**, 1–41 (1995).
54. S. Izadi, A. V. Onufriev, Accuracy limit of rigid 3-point water models. *J. Chem. Phys.* **145**, 074501 (2016).